Article

Cell Reports

A Mutation in the Borcs7 Subunit of the Lysosome Regulatory BORC Complex Results in Motor Deficits and Dystrophic Axonopathy in Mice

Graphical Abstract

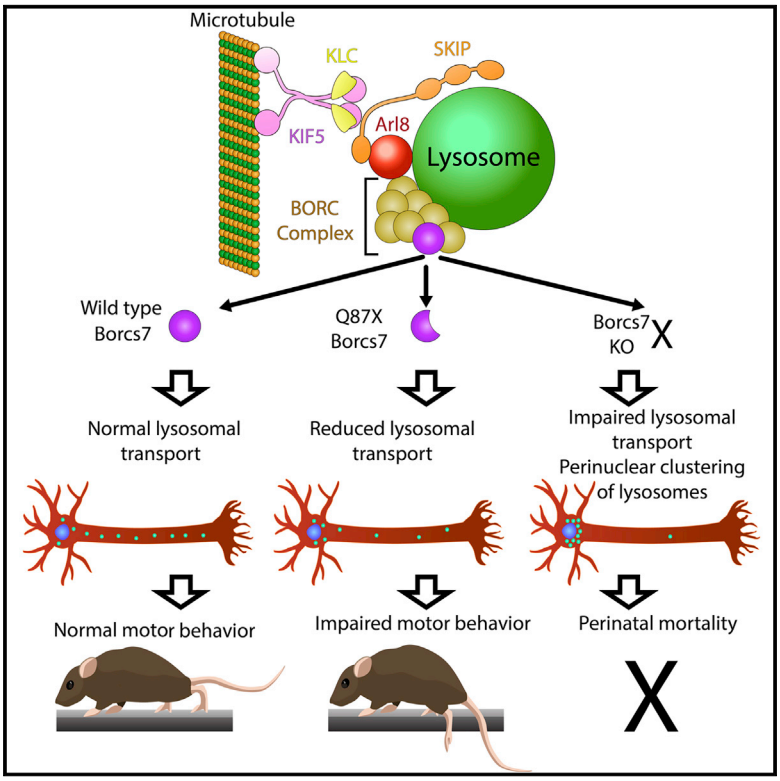

Highlights

- Borc7 is essential for anterograde transport of lysosomes in neurons
- Loss of Borcs7 causes juxtanuclear clustering of lysosomes and perinatal mortality
- A truncation mutation in Borcs7 causes reduced lysosomal transport in neurons
- Truncated Borcs7 causes progressive axonal dystrophy and impaired motor function

Authors

John N. Snouwaert, Rachel J. Church, Leigh Jania, ..., Sheryl S. Moy, Damaris N. Lorenzo, Beverly H. Koller

Correspondence

bkoller@email.unc.edu

In Brief

BORC is a multisubunit complex that regulates lysosomal positioning. Snouwaert et al. report that a truncation mutation in Borcs7, a subunit of this complex, results in reduced lysosomal transport, progressive axonal dystrophy, and impaired motor function in mice. Loss of Borcs7 causes juxtanuclear clustering of neuronal lysosomes and perinatal mortality.

Snouwaert et al., 2018, Cell Reports *24*, 1254–1265
July 31, 2018
https://doi.org/10.1016/j.celrep.2018.06.118

CellPress

OPEN ACCESS
CellPress

Cell Reports
Article

A Mutation in the Borcs7 Subunit of the Lysosome Regulatory BORC Complex Results in Motor Deficits and Dystrophic Axonopathy in Mice

John N. Snouwaert,[1,9] Rachel J. Church,[1,9] Leigh Jania,[1] MyTrang Nguyen,[1] Matthew L. Wheeler,[1] Andrew Saintsing,[1] Piotr Mieczkowski,[2] Fernando Pardo Manuel de Villena,[3] Diane Armao,[4,5,6] Sheryl S. Moy,[7] Damaris N. Lorenzo,[8,10] and Beverly H. Koller[1,10,11,*]

[1]Department of Genetics, University of North Carolina at Chapel Hill, Chapel Hill, NC 27599, USA
[2]High Throughput Sequencing Facility, School of Medicine, University of North Carolina at Chapel Hill, Chapel Hill, NC 27599, USA
[3]Department of Genetics and Lineberger Comprehensive Cancer Center, University of North Carolina at Chapel Hill, Chapel Hill, NC 27599, USA
[4]Department of Radiology, UNC Healthcare System, Chapel Hill, NC 27599, USA
[5]Department of Pathology and Laboratory Medicine, University of North Carolina School of Medicine, Chapel Hill, NC 27599, USA
[6]Department of Physician Assistant Studies, Elon University, Elon, NC 27244, USA
[7]Department of Psychiatry and Carolina Institute for Developmental Disorders, University of North Carolina at Chapel Hill, Chapel Hill, NC 27599, USA
[8]Department of Cell Biology and Physiology, University of North Carolina at Chapel Hill, Chapel Hill, NC 27599, USA
[9]These authors contributed equally
[10]Senior author
[11]Lead Contact
*Correspondence: bkoller@email.unc.edu
https://doi.org/10.1016/j.celrep.2018.06.118

SUMMARY

Lysosomes play a critical role in maintenance of the integrity of neuronal function, and mutations in genes that contribute to lysosome formation, transport, and activity are associated with neurodegenerative disorders. Recently, the multisubunit complex, BLOC-one-related complex (BORC), has been shown to be involved in positioning lysosomes within the cytoplasm, although the consequences of altered BORC function in adult animals have not been established. We show that a spontaneous truncation mutation in the mouse *Borcs7* gene, identified through whole-genome sequencing followed by genetic complementation, results in progressive axonal dystrophy with dramatic impairment of motor function. Furthermore, mice homozygous for deletion of the entire *Borcs7* coding sequence die shortly after birth, and neurons cultured from these animals show impaired centrifugal transport of lysosomes. This identifies BORCS7 as a central factor in axonal transport of lysosomes and a possible target for improving disease-related disturbances in this important function.

INTRODUCTION

Because of the relatively large fraction of cytoplasmic volume distributed throughout their axonal and dendritic processes, neurons are particularly susceptible to accumulation of cellular waste, which cannot be diluted during cell division as it is in mitotic cells. This problem is magnified in neurons with particularly long processes, such as upper motor neurons, in which axonal cytoplasm may account for 99% of cellular volume. Normal lysosomal function is therefore particularly important for neuronal health, and this is evidenced by the relatively large number of neurodegenerative disorders that have been linked to mutations that disrupt autophagy or the endosomal pathway (Blackstone et al., 2011; Menzies et al., 2017; Navone et al., 2015). Disorders linked to abnormal lysosome function include Parkinson's disease (Abeliovich and Gitler, 2016; Haidar and Timmerman, 2017), Huntington's disease (Fraldi et al., 2016), Alzheimer's disease (Martini-Stoica et al., 2016), amyotrophic lateral sclerosis (ALS) (Kiriyama and Nochi, 2015), hereditary spastic paraplegia (HSP) (Ebrahimi-Fakhari et al., 2016; Schreij et al., 2016), and neuroaxonal dystrophy (NAD) (Walkley et al., 2010).

In addition to mutations affecting lysosomal enzyme activity and endoplasmic-reticulum-associated endosomal tubule fusion, mutations affecting lysosomal mobility within the neuronal cytoplasm have also been associated with neurodegenerative disease. Distribution and movement of organelles, including lysosomes, are determined partly by their transport along microtubules. Although anterograde transport in axons is driven by a variety of kinesins, retrograde transport in mammals is dependent on a single dynein. A defect in retrograde transport of lysosomes along axons has been shown to result in motor axon degeneration in mice carrying the legs at odd angles (Loa) mutation. Mice heterozygous for this mutation, which introduces a single-amino-acid mutation into the dynein heavy chain, show decreases in both dynein processivity and run lengths for lysosomes (Ori-McKenney et al., 2010). Mutations in a zebrafish ortholog of KIF5A, which encodes the neuronal kinesin heavy chain, have been shown to result in deficits in anterograde transport of mitochondria in axons followed by neurodegeneration

(Campbell et al., 2014). Mutations in the *KIF5A* gene are associated with HSP, Charcot-Marie-Tooth disease (Crimella et al., 2012), and ALS (Nicolas et al., 2018).

Anterograde transport of lysosomes into the axon has recently been shown to be driven by an ensemble composed of kinesin-1, SKIP, Arl8, and the eight subunits of the BORC (for BLOC-one-related complex). These subunits consist of BLOS1, BLOS2, and Snapin, all of which are common to BLOC1, plus KXD1, LOH12CR1/myrlysin, C17orf59/lyspersin, C10orf32/diaskedin, and MEF2BNB. These subunits are also referred to, respectively, as BORCS (1–8; Pu et al., 2015). Interference with the function of the BORC decreases lysosome transport into the axon, and its function is required for maintenance of axonal growth cone dynamics and autophagosome clearance (Farías et al., 2017).

We report here the characterization of a mouse carrying a mutation resulting in expression of a truncated version of the BORC subunit BORCS7 (C10orf32/diaskedin), which results in a phenotype with many similarities to human HSP.

RESULTS

Identification and Initial Phenotypic Characterization of a Mouse Line with Loss of Hind Limb Motor Coordination

The phenotype associated with the truncation mutation in *Borcs7* was initially identified as the result of a spontaneous mutation within our breeding program. Affected animals displayed an altered gait that became more severe with age. These animals could be further distinguished from littermates because of hind limb clasping upon suspension by the tail. This reflex is commonly used as a marker of disease progression in a number of mouse models of neurodegeneration, including neurodegeneration resulting from loss of autophagy (Komatsu et al., 2006). Young affected females were fertile and had normal-sized litters. Young males could mate, but with the progressive loss of motor coordination, their fertility declined by 15 weeks. To verify the inheritance pattern of the phenotype and to rule out the contribution of an infectious agent to the phenotype, sperm were collected from an affected male and used to fertilize C57BL/6 oocytes. The fertilized oocytes were returned to a foster mother housed in a second specific pathogen-free facility. No disease was observed in any of the offspring born to these surrogate dams. However, when these mice were intercrossed, approximately 25% of the offspring displayed the same motor deficits. This indicated that the phenotype was the result of a single mutant locus with recessive inheritance.

Histological Analysis

To determine whether the changes in motor coordination observed in mutant mice resulted from pathological alterations, we examined the cell bodies of motor neurons within the ventral horns of these animals by light microscopy. Sections were prepared from the lumbar spinal cord and stained with cresyl violet and Luxol Fast Blue (Figures 1A–1C). Motor neuron cell bodies within the ventral horn were generally well preserved. At both low and high magnifications, spherical bodies staining intensely blue were observed in sections prepared from the mutant mice, suggesting the presence of dystrophic axons. Similar dystrophic axons were also observed in the sciatic nerve. Numerous swollen axons were present in ultra-thin sections prepared from the lumbar cord of mutant animals. The distribution of spheroidal swellings was diffuse, including both gray matter and white matter, and could be detected in both motor and sensory tracts. In the mutant animals, swollen axons were pronounced and numerous, affecting both myelinated and unmyelinated fibers (Figures 1D–1F). Many of the spheroids showed dense accumulations of organelles in various stages of degeneration. Importantly, tubulovesicular elements forming an anastomosing, curvilinear network of delicate membrane structures with lumens were identified in a number of the swollen axons (Figure 1G).

Analysis of Behavior and Motor Deficits in Affected Mice

Behavioral testing was performed in control (n = 10) and affected (n = 9) mice over a one-month interval. No significant difference in weight was observed between the groups over the duration of the study. The mutant mice were easily distinguishable on the wire-hang task for grip strength, with a significant difference being observed, both in the latency to fall and in the overall coordination score, at both 4 and 8 weeks of age (Figures 2A and 2B). Similarly, a significant difference in performance was observed when the motor coordination and learning of the mice were examined using the rotarod, which was already manifested at the earliest time point tested (Figure 2C). However, similar to control animals, their performance improved over the trial period.

The exploratory activity in a novel environment was assessed by one-hour trials in an open-field chamber. Mice were given two one-hour tests for locomotor and vertical activity: one at 5 weeks and one at 8 weeks (Figures 2D and 2E). Interestingly, at 5 weeks of age, the mutant mice were significantly hyperactive, showing increased general activity in the beginning intervals of the test. By the time of the second test, these differences between the genotypes were no longer evident, perhaps reflecting a balance between hyperactivity and changes in motor activity. A different pattern emerged with the measure for rearing movement (Figures 2F and 2G). In this case, no significant difference was observed between mice at 5 weeks of age. However, by the second test, the mutant mice showed a striking reduction in the ability to rear, consistent with the loss of hind limb strength, suggesting that hind limb ataxia emerges during the adolescent period in the mutant animals.

The acoustic startle test can be used to assess auditory function and sensorimotor gating. The test is based on the measurement of the reflexive whole-body flinch or startle response that follows exposure to sudden noise. A small but significant reduction in the startle amplitudes of the mutant mice was seen at six weeks, but the difference was no longer observed in subsequent tests (Figures S1A–S1D; Supplemental Experimental Procedures). The ability of the prepulse to inhibit the startle response did not differ between groups. The Morris water maze (Figures S1E and S1F; Supplemental Experimental Procedures) was used to assess swimming ability in the mice, as well as their ability to respond to visual cues used to identify the location of the escape platform. In contrast to the overt deficits found in rotarod performance and ability to rear, the mutant mice had only mild changes in measures from the water maze, with longer latencies to the escape platform on the third day of testing, and a

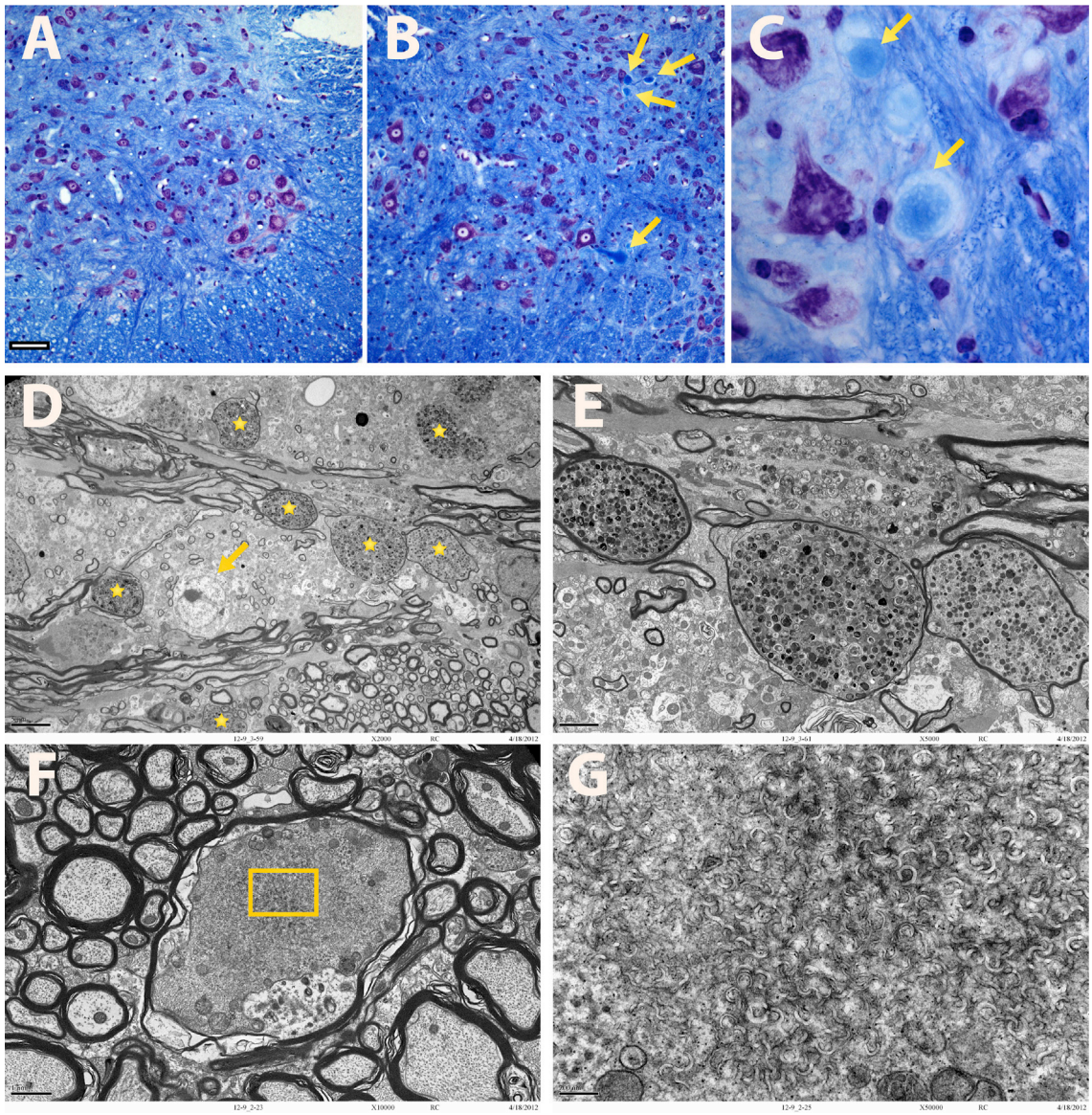

Figure 1. Light Microscopy of Spinal Cord from Wild-Type Mice and Q87X Mice and Ultrastructural Features in Axons of the Spinal Cord of a 9-Month-Old Q87X Mouse

Perfusion-fixed spinal cords were embedded in paraffin, transversely sectioned, and stained with Luxol Fast Blue/cresyl violet, which highlights the myelin sheath and neuronal cell bodies, respectively. Motor neuron cell bodies, easily identified by their prominent nucleoli and Nissl substance, are abundant in the ventral horn of both mutant and normal mice.

(A–C) Intense, densely staining spherical bodies (arrows) are observed in sections from the mutant animals (B and C), but not identified in the normal mice (A). The scale bar represents 100 μm.

(D) Numerous spheroids (stars) are identified and are characterized by thinly myelinated and unmyelinated axonal swellings. Scale bar, 5 μm. Neuronal cell bodies (arrow) appear intact (2,000×).

(E) Higher magnification reveals axonal swellings surrounded by disproportionately thin myelin sheaths and distended by massive accumulations of filaments, vesicles, vacuoles, membrane-bound dense bodies, mitochondria, and amorphous matrix (5,000×). Scale bar, 2 μm.

(F) Greatly enlarged axonal swelling with attenuation of the myelin sheath and numerous marginated mitochondria surrounding dense aggregates of degenerating organelles (10,000×). Scale bar, 1 μm.

(G) High magnification (region indicated by rectangle in C) revealing the extensive curvilinear-shaped, tubulovesicular structures that comprise the predominant feature of the dystrophic axon (50,000×). Scale bar, 200 nm.

non-significant trend for lower swimming speeds. Overall, the results show that the mutant mice had the greatest impairment in motor tasks dependent on hind limb function.

Identification of the Mutant Locus

The genetic composition of the mouse population in which the phenotype was observed was 129S6/C57BL/6/DBA/2 at a

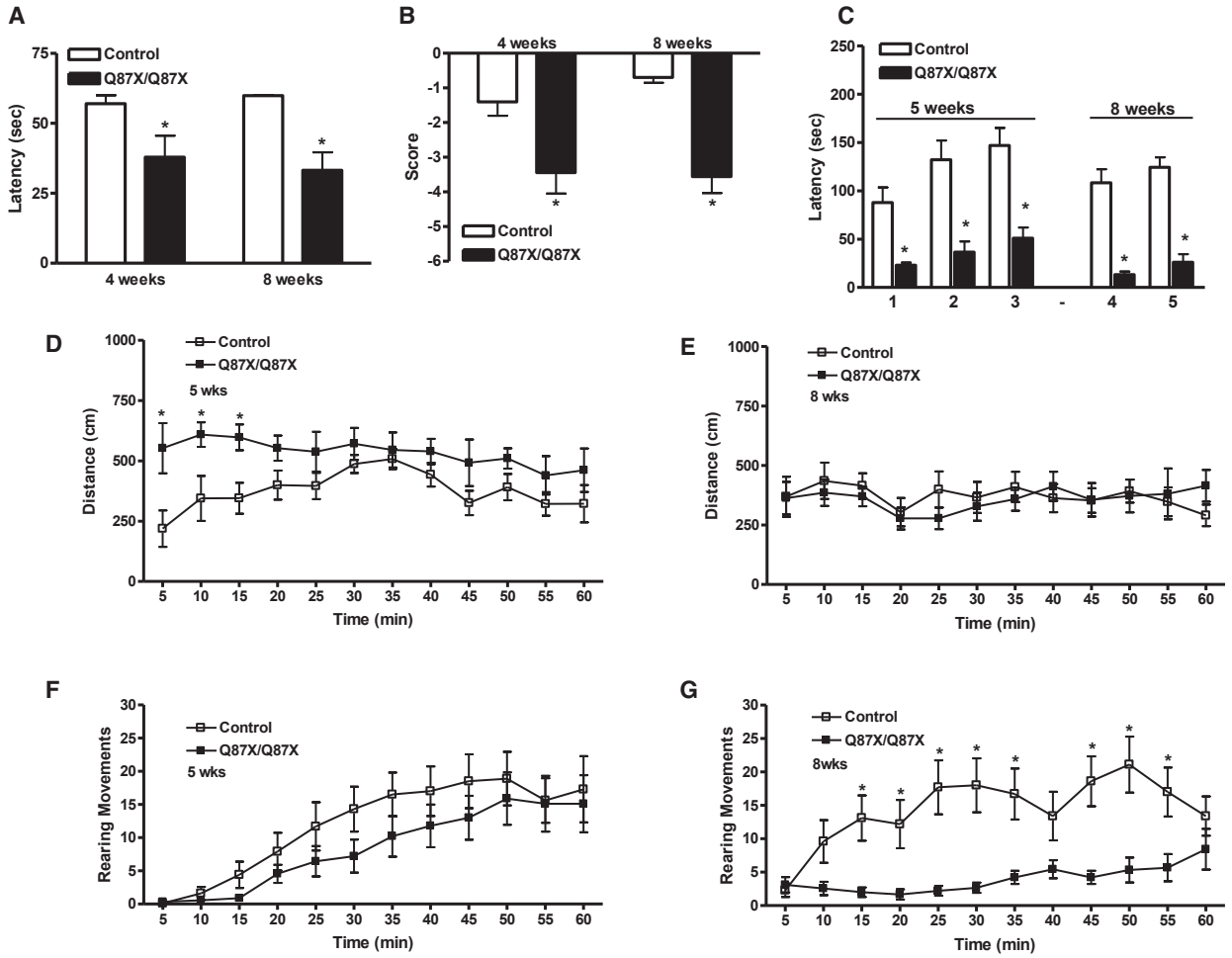

Figure 2. Behavioral Analysis in Mice Aged 4 or 5 Weeks and 8 Weeks

The paw grip test for assessing strength and coordination was conducted at 4 and 8 weeks of age. Mice were placed on a wire cage rack, which was subsequently upturned.

(A and B) Latency to fall (A) and coordination (B) were recorded. Time to fall and coordination were significantly attenuated in mutant animals compared to controls (*$p < 0.05$ for both).

(C) Testing was conducted on an accelerating rotarod at 5 and 8 weeks of age to assess motor coordination and learning. Three trials were conducted with 45 s between each trial. rpm (revolutions per minute) was set at an initial value of 3, with a progressive increase to a maximum of 30 rpm across 5 min (the maximum trial length). Time to fall was measured. Latency was significantly reduced in affected animals during all trials (*$p < 0.01$) compared to controls (control n = 10; Q87X/Q87X n = 9). Locomotor activity in a novel environment was examined over an hour time course.

(D–G) Photo beams crossed during 5-min intervals were quantified for both ambulation (D and E) and rearing (F and G). No difference was observed in distance traveled between control and mutant animals at 8 weeks; however, affected animals demonstrated significantly fewer rearing motions across many time intervals when the mice were tested at 8 weeks, but not at 5 weeks. Bars represent SEM; *$p < 0.05$.

2:1:1 ratio (data not shown). SNP analysis on DNA from 9 affected and 6 unaffected animals showed that all affected animals were homozygous for 129 alleles over a 20.7-MB region on mouse chromosome 19, extending from rs6291559 to rs3023496. We verified the location of the mutant locus by using a breeding strategy to isolate this segment of 129 DNA. An affected female was crossed with a BALB/cByJ male. Offspring were then intercrossed, and an affected female was identified by monitoring for clasping upon suspension by the tail and bred again to a BALB/cByJ male. After another similar round of breeding, DNA was collected from the N3-affected animals and analyzed for the continued presence of the 129S6-derived segment of Ch19. This confirmed the linkage of this segment of DNA to the motor coordination defect in the mouse line. Further backcrossing onto the BALB/cByJ genetic background reduced the candidate region to a segment of DNA defined by 19q46.102–19q46.269, a region containing approximately 30 genes.

To identify potential mutations, whole-genome sequence analysis was carried out on a mouse homozygous for the mutant phenotype. The affected mouse was homozygous for a single base pair substitution in exon 4 of *Borcs7*, which generates the nonsense mutation Q87X, resulting in a truncated protein lacking 18 amino acids at its C terminus. The Q87X mutation destroys an

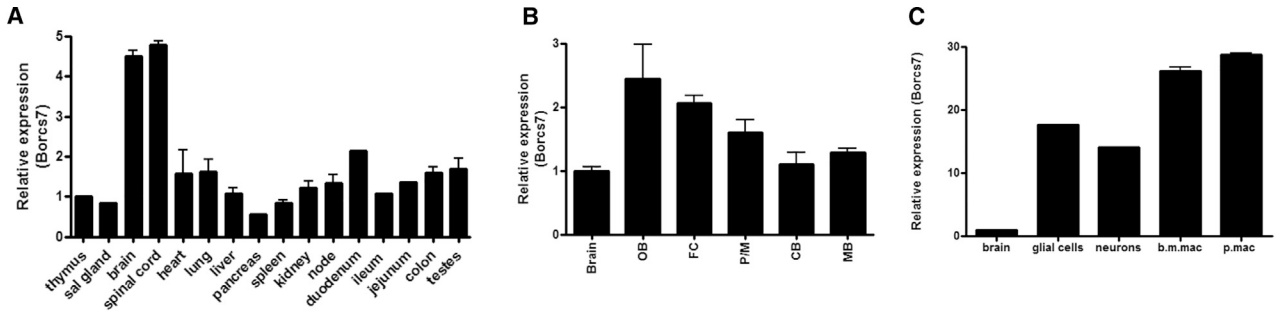

Figure 3. Expression of *Borcs7* in Tissues and Primary Cells

Expression was assessed by qPCR, normalizing to 18S RNA.

(A) Relative expression of *Borcs7* in a number of tissues expressed as fold change relative to the expression level measured in thymus.

(B) The expression in the various tissues and regions of the brain are shown relative to the level in the RNA prepared from brain. CB, cerebellum; FC, frontal cortex; MB, midbrain; OB, olfactory bulb; P/M, pons/medulla.

(C) Comparison of *Borcs7* expression in brain with that in isolated glial cells, neurons, and macrophages. b.m. mac, bone marrow macrophages; p. mac, peritoneal macrophages.

Bars represent SEM.

Xmn1 restriction site, allowing easy verification of the mutation by Southern analysis in additional affected animals. We refer to the protein product of this mutant locus as BORCS7-Q87X and mice homozygous for this mutation as *Borcs7*$^{Q87X/Q87X}$.

Verification that the Truncation Mutation in Borcs7 Leads to the Observed Loss of Motor Function

To begin to link the Q87X mutation in *Borcs7* to the phenotype observed in homozygous mice, we examined the relative levels of *Borcs7* expression from the endogenous mouse locus in multiple tissues of wild-type mice (Figure 3A). Consistent with the obvious effects of the truncation mutation on motor functions, we found that *Borcs7* expression in brain and spinal cord was approximately two times higher than in any of the other tissues examined. Comparison of relative *Borcs7* expression levels in various brain regions showed the highest expression in the olfactory bulb and frontal cortex (Figure 3B). We next compared levels of *Borcs7* expression in multiple cell types to that in the whole brain (Figure 3C). Interestingly, whereas *Borcs7* is expressed abundantly in both neurons and glial cells, the highest expression levels were detected in macrophages. Thus, the expression pattern, although consistent with the phenotype, does not support an exclusive function for this protein in neurons.

To prove that the nonsense mutation in *Borcs7* is responsible for the dramatic changes in mouse motor activity observed in the *Borcs7*$^{Q87X/Q87X}$ mice, we designed a genetic complementation assay. A targeting plasmid was designed which, upon recombination with the mouse genome, should remove the entire 13.3 kb of the mouse gene, including the entire coding sequence (Figure S1; Supplemental Experimental Procedures). The targeting vector was introduced into embryonic stem cells (ESCs), targeted colonies were identified by PCR followed by Southern analysis, and two independent lines were introduced into B6 blastocysts. Chimeras with high ESC contribution were bred directly to females heterozygous for the truncation mutation, referred to as *Borcs7*$^{+/Q87X}$. Pups generated by this cross that carried the Q87X allele were identified by Southern blot analysis using a probe designed to detect loss of the Xmn1 site. The presence of the null allele was determined by PCR. Three mice carrying one copy of the Q87X mutation and one null allele, referred to as *Borcs7* $^{Q87X/-}$, were identified in the first two litters, and these were compared to *Borcs7*$^{Q87X/+}$ littermates. As can be seen in Figure 4, the loss of the wild-type *Borcs7* allele at the paternal locus is sufficient to result in a phenotype in the mice with a single copy of the Q87X allele at the maternal locus. This identifies *Borcs7* as the gene carrying the mutation that confers the phenotype observed in our original mouse population.

Mice Homozygous for the Null *Borcs7* Allele Die Perinatally

Mice homozygous for the null *Borcs7* allele, referred to as *Borcs7*$^{-/-}$, were present in litters at expected Mendelian ratios (data not shown). Pups were normal in size and could not be distinguished from littermates by appearance or evaluation of organ systems on necropsy. Histologically, no gross defect in the development of organs was noted. However, the pups failed to feed and were removed from the nest by the dams, and all *Borcs7*$^{-/-}$ pups died within 12 hr of birth. The fate of these mice indicates that the truncation mutation produced by the Q87X allele retains some level of function and that *Borcs7* plays a crucial role in the normal physiology of the animals.

Lysosomal Localization Is Altered in BORCS7-Deficient Neurons

Studies using short hairpin RNA (shRNA)-mediated knockdown of BORC components in cultured rat hippocampal neurons have identified a role for the BORC in the polarized transport of lysosomes into the axon. To examine the effects of BORCS7 deficiency on lysosomal transport, we examined lysosomal distribution and dynamics in cultured cortical neurons and liver macrophages prepared from 15.5-day-old embryos. Loss of BORCS7 did not alter the plating efficiency or survival of the cells, and no difference was apparent in the gross appearance of the neurons or macrophages. This is consistent with the grossly normal development of the nervous and other organ systems of these animals. To examine the effects of BORCS7

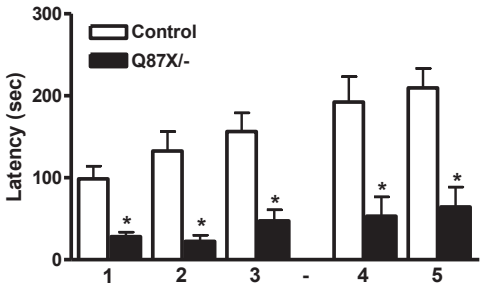

Figure 4. Latency to Fall from an Accelerating Rotarod

The performance of Borcs7$^{Q87X/-}$ mice was compared to that of *Borcs7*$^{+/-}$ and *Borcs7*$^{Q87X/+}$ littermates (controls) placed on an accelerating rotarod. Tests 4 and 5 were carried out 48 hr after the first three tests. N = 7 for controls and N = 3 for Borcs7$^{Q87X/-}$ mice. Despite the small group size, the deficit in motor coordination of the compound heterozygous animals was easily discerned. Error bars represent SEM; *p < 0.05.

deficiency on lysosomal distribution, lysosomes were visualized by immunostaining for LAMP1 (Figures S3 and S4). In fetal liver macrophages, the distribution of lysosomes was not visibly altered by loss of BORCS7. In contrast, lysosomes in cultured cortical neurons from *Borcs7*$^{-/-}$ mice displayed a dramatically different distribution, clustering primarily in the soma of cells. To verify this observation and determine whether the Q87X mutation similarly altered neuronal distribution of lysosomes, cortical neurons were prepared from *Borcs7*$^{+/+}$, *Borcs7*$^{-/-}$, and *Borcs7*$^{Q87X/Q87X}$ mice, and after 6 days in culture (*in vitro* day 6 [DIV6]), cells were transfected with vectors carrying transgenes expressing fluorescently tagged versions of LAMP1 and KIF5A (Figure S5). Microscopic examination of axons of the transfected neurons revealed extensive co-localization of the tagged proteins throughout the length of the axons in *Borcs7*$^{+/+}$, but not in *Borcs7*$^{-/-}$, neurons. In contrast, we observed a more diffuse distribution of mScarlet-KIF5A in Borcs7−/− axons, which together with the significant reduction in LAMP1-GFP particles at the distal axon precluded the evaluation of the effect of total Borcs7 loss on KIF5A-lysosome association.

Lysosomal distribution in live neurons was quantified by live imaging of cortical neurons from *Borcs7*$^{+/+}$, *Borcs7*$^{Q87X/Q87X}$, and *Borcs7*$^{-/-}$ mice expressing GFP-LAMP1. After live imaging and establishment of the location of lysosomes, cells were stained for ankyrin-G (AnkG), a marker for the axon initial segment, allowing identification of axonal and dendritic processes (Figure 5A). As expected, the number of lysosomes in the axons of *Borcs7*$^{-/-}$ neurons was extremely low, resulting in an elevated dendrite-to-axon ratio (Figures 5A, 5C, and 5D). A modest but significant decrease in the number of lysosomes in axons relative to controls was observed in the *Borcs7*$^{Q87X/Q87X}$ axons (Figures 5A and 5D). This decrease in axonal lysosomes resulted in a significant increase in the dendrite-to-axon ratio in cells expressing the truncated protein (Figure 5C). Transfection of *Borcs7*$^{-/-}$ neurons with a vector expressing hemagglutinin (HA)-tagged wild-type *Borcs7* rescued the abnormal lysosome distribution observed in these neurons (Figure 5).

Mutations in BORCS7 Alter Lysosomal Dynamics

The effects on lysosomal dynamics of BORCS7 deficiency or homozygosity for the Q87X mutation were determined in DIV7 cortical neuron cultures. Relative to wild-type controls, *Borcs7*$^{-/-}$ neurons showed a significant reduction in anterograde velocity of LAMP1-GFP-labeled lysosomes (Figures 6A and 6B). *Borcs7*$^{Q87X/Q87X}$ neurons showed decreased anterograde velocity relative to *Borcs7*$^{+/+}$ neurons, but the effect was smaller than that observed in *Borcs7*$^{-/-}$ neurons. *Borcs7*$^{Q87X/Q87X}$ and *Borcs7*$^{-/-}$ neurons also showed reductions in both anterograde and retrograde lysosomal run length (Figure 6C). Transport deficits and lysosomal localization at the distal axon could be rescued by expression of wild-type BORCS7, demonstrating a requirement for this BORC complex subunit for axonal lysosomal dynamics and distribution (Figure 6).

To examine whether BORCS7 was required for axonal transport of other organelles, we monitored the dynamics of mitochondria and synaptic vesicles by transfecting *Borcs7*$^{+/+}$, *Borcs7*^{Q87XQ87X}, and *Borcs7*$^{-/-}$ cortical neurons with vectors expressing mito-GFP or synaptophysin-YFP, respectively. Loss of BORCS7 had no detectable effect on the transport of mito-GFP-positive vesicles, and a small but significant difference was observed in anterograde run length of synaptophysin-YFP-positive vesicles in *Borcs7*$^{-/-}$ neurons relative to *Borcs7*$^{+/+}$ and *Borcs7*^{Q87XQ87X} neurons (Figure S6).

The Q87X Mutation Does Not Affect Expression Levels of *Borcs7* mRNA but Decreases Stability of BORCS7

RNA was isolated from the spinal cord of *Borcs7*$^{+/+}$ and *Borcs7*$^{Q87X/Q87X}$ mice to determine whether the missense mutation also affected transcription and/or mRNA stability (Figure 7A). We also examined expression levels of the neighboring gene *As3mt* (arsenic [+3 oxidation state] methyltransferase). Studies have identified a transcript that includes codons of *Borcs7* and *As3mt*, and both of these genes have been identified as molecular risk factors in the 10q24.32 schizophrenia-associated locus (Li et al., 2016). The Q87X mutation had no detectable effect on the expression level of either gene as determined by qPCR analysis.

It is possible that the phenotypic effects of the Q87X truncation mutation could result in part from a decrease in stability of the mutant protein. As extensive testing of a commercially available C10orf32 polyclonal antibody (PA5-77186 Invitrogen) against BORCS7 indicated that it was unable to specifically recognize this target, we prepared vectors capable of expressing either HA-tagged wild-type BORCS7 or HA-tagged BORCS7-Q87X. The vectors were transfected into HEK293T cells, and the half-life of the tagged proteins was measured via a cycloheximide chase assay. Our results indicated that the truncation associated with the Q87X mutation reduced the half-life of BORCS7 by about 75% compared to the wild-type control (Figures 7B and 7C).

The Q87X Mutation Does Not Disrupt the Association of Borcs7 with Snapin

To examine whether truncation of the BORCS7-Q87X protein prevents it from interacting normally with the BORC, we co-expressed GFP-Snapin and either HA-tagged BORCS7 or

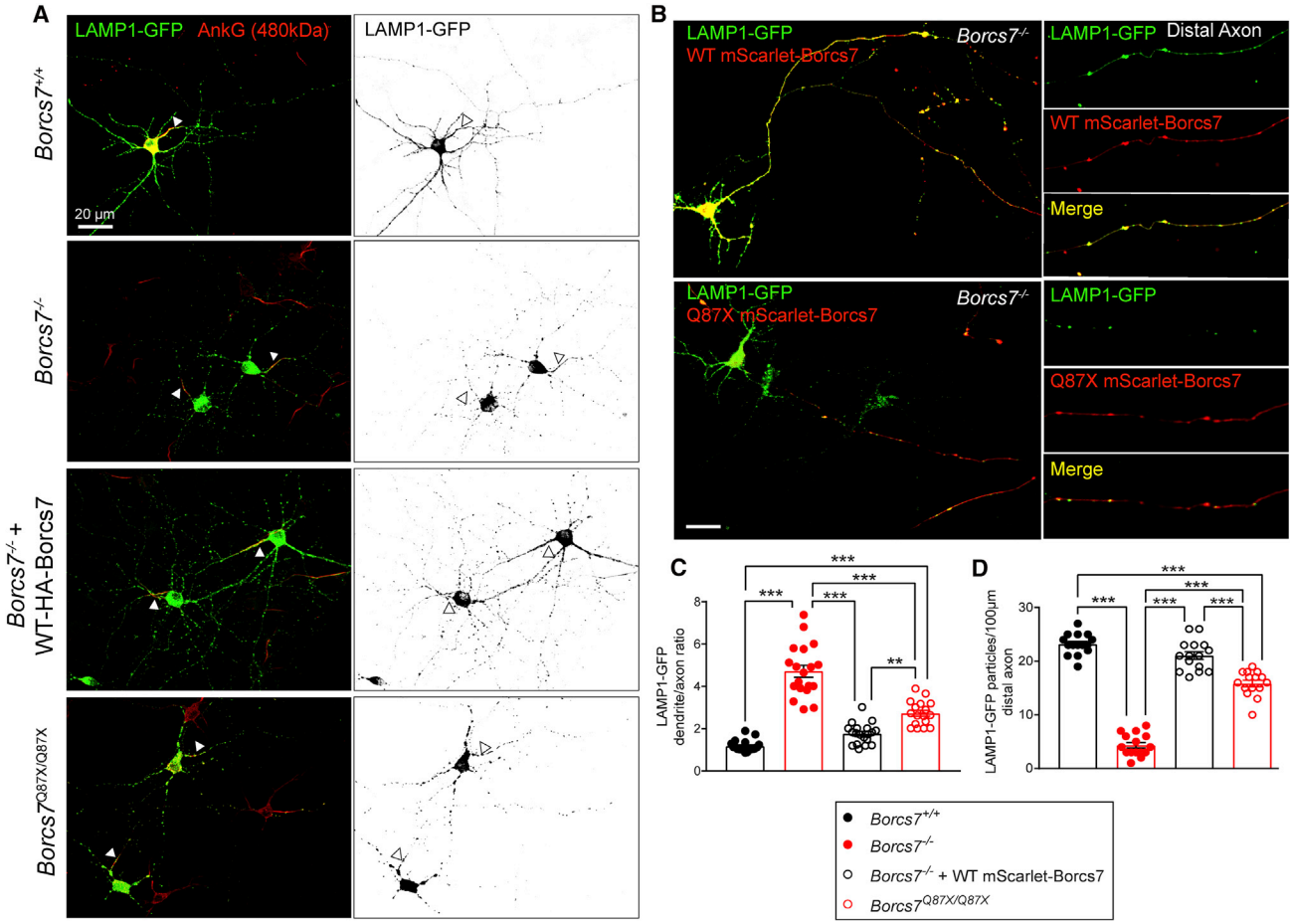

Figure 5. Effect of Borcs7 Genotype on LAMP1-GFP Distribution in Neurons

(A) Representative images of DIV8 hippocampal neurons of each genotype expressing LAMP1-GFP. Axons were identified by staining for ankyrin-G (AnkG 480 kDa isoform; red channel staining).

(B) Distribution of GFP-labeled lysosomes and mScarlet-labeled wild-type (WT) or BORCS7-Q87X. Right panels show LAMP1-GFP distribution and co-localization with mScarlet-BORCS7 at the distal axon. Scale bar, 20 μm.

(C) Dendrite to axon ratio of LAMP1-GFP distribution in neurons.

(D) Number of LAMP1-GPF-labeled vesicles in 100 μm of distal axon.

Data represent means ± SEM. *$p < 0.05$; **$p < 0.01$; ***$p < 0.001$; one-way ANOVA with Tukey's post test.

BORCS7-Q87X in HEK293T cells. BORCS7 and associated proteins were immunoprecipitated from lysate prepared from transfected cells with an antibody against the HA tag. Western blot analysis of precipitated protein with an antibody against GFP or HA indicated that BORCS7-Q87X protein is similar to wild-type (WT) BORCS7 in its ability to associate with Snapin.

DISCUSSION

In the present study, we report the finding of motor deficits as well as morphologic neurodegenerative changes in mice homozygous for a spontaneous, nonsense mutation (Q87X) in *Borcs7*, a member of the multisubunit BORC responsible for regulation of lysosome positioning. By 5 weeks of age, *Borcs7*$^{Q87X/Q87X}$ mice displayed impaired motor performance in several tests, including the wire hang test for grip strength and the rotarod test for coordination. Affected mice also displayed a significant deficit in their ability to rear. The motor deficits observed in mutant mice were accompanied by morphologic abnormalities within the spinal cord. By both light and electron microscopy, examination of the spinal cord revealed relatively intact neuronal cell bodies, along with abundant and pronounced spheroidal axonal swellings. Dystrophic axons were distended by degenerating organelles, amorphous matrix material and tubulovesicular structures. Such abnormal accumulations within swollen axons are pathological features observed in axonopathies associated with a variety of disorders, including NAD (Schmidt et al., 1997), and have also been observed in a rat model of HSP (Watanabe et al., 2013). These features have also been observed in axonopathies associated with trauma, ischemia, and aging. A number of reports indicate that dysfunction of the autophagy-lysosome pathway can contribute to axonal swellings (Kragh et al., 2012; Yang et al., 2009) by interfering with the neuron's ability to degrade and/or remove subcellular materials or organelles in

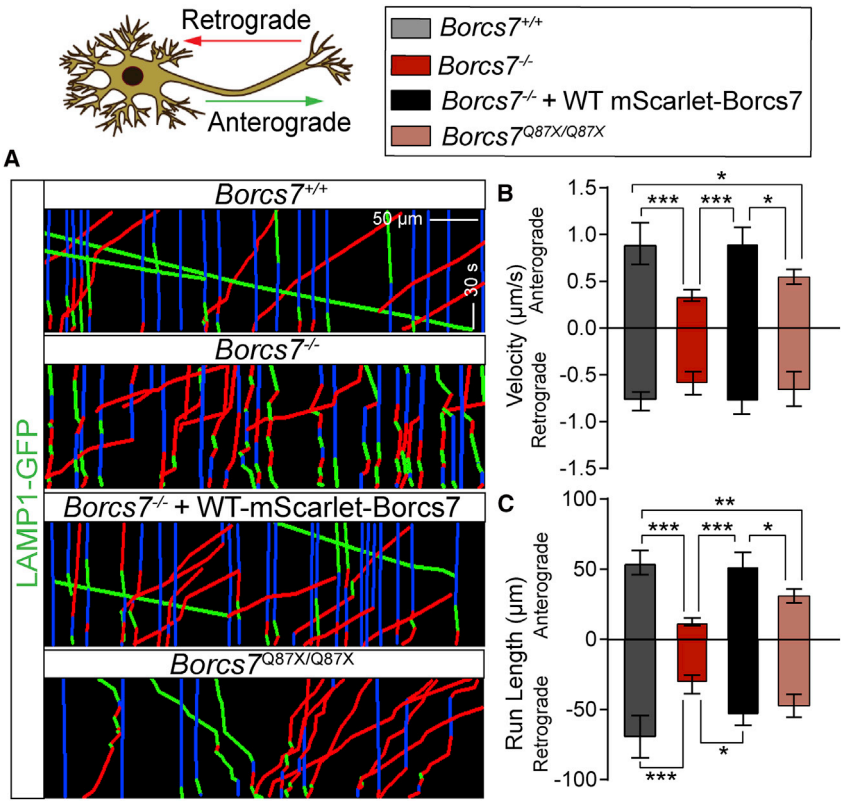

Figure 6. Effect of Borcs7 Genotype on Lysosome Dynamics in Neurons

(A) Kymograph of LAMP1-GFP dynamics in axons of the indicated genotypes. GFP-labeled lysosomes show normal motility post rescue with WT mScarlet-BORCS7.

(B and C) Velocity (B) and run length (C) of LAMP1-GPF-labeled vesicles. Data represent means ± SEM. *p < 0.05; **p < 0.01; ***p < 0.001; one-way ANOVA with Tukey's post test.

the distal parts of axons. Together with the relative sparing of the soma of the motor neurons, these findings are consistent with the hypothesis that the mutation carried in this line of mice results in neuroaxonal dystrophy with morphologic features similar to human NAD.

The crucial role played by BORCS7 in normal cellular physiology is suggested by the fact that it is evolutionarily conserved, with orthologs found in both vertebrates and invertebrates. The importance of the BORC complex for normal development is indicated by the embryonic lethal phenotype in mice resulting from disruption of the Snapin (Tian et al., 2005), BLOS1 (Zhang et al., 2014), or BLOS2 (Guardia et al., 2016; Zhou et al., 2016) subunits of the BORC, as well as by the perinatal lethal phenotype that we observed in mice homozygous for inactivation of the *Borcs7* gene. Previous studies indicate that disruption of function of any of the various members of the BORC, including BORCS7, results in juxtanuclear collapse of the lysosome population (Pu et al., 2015). Furthermore, the BORC has been shown to play a role in anterograde transport of lysosomes along the axon (Farías et al., 2017). Given the importance of bidirectional movement of lysosomes within the cytoplasm for a number of cellular processes, such as autophagy, metabolic signaling, plasma membrane repair, cell adhesion, and cell migration (Korolchuk et al., 2011; Reddy et al., 2001; Mrakovic et al., 2012; Pu et al., 2015), it is not surprising that deficiency in any one of the subunits of the BORC should impact the development of a number of organ systems and result in embryonic or perinatal lethality.

To determine the effect of BORCS7 deficiency on lysosome positioning, we compared the distribution of LAMP1-positive vesicles in cells derived from BORCS7-deficient mice and wild-type controls. Whereas BORCS7 deficiency caused LAMP1-positive vesicles to cluster in the soma of cortical neurons, the distribution of these vesicles in BORCS7-deficient macrophages was similar to that in wild-type controls. Further investigation will be required to determine whether this is because BORCS7 does not play the same role in lysosomal localization in macrophages as it does in neurons.

To allow a more detailed examination of the effects of the absence or truncation of the BORCS7 protein on lysosomal transport in neurons, we transfected cortical neurons from *Borcs7*$^{+/+}$, *Borcs7*$^{-/-}$, and *Borcs7*$^{Q87X/Q87X}$ mice with genes expressing fluorescently tagged versions of LAMP1 and KIF5A. Microscopic examination of axons of the transfected neurons revealed extensive co-localization of the tagged proteins throughout the length of the axons in both *Borcs7*$^{+/+}$ and *Borcs7*$^{Q87X/Q87X}$ neurons, but not in *Borcs7*$^{-/-}$ neurons. This suggests, as might be expected based on the phenotypes of *Borcs7*$^{Q87X/Q87X}$ and *Borcs7*$^{-/-}$ mice, that any effects of truncation of BORCS7 on lysosomal positioning are subtler than those caused by complete BORCS7 deficiency. This was confirmed by quantitative analysis of lysosomal positioning in live neurons, which revealed a significant decrease in the density of LAMP1-positive vesicles in the distal axons of *Borcs7*$^{-/-}$ neurons relative to those of wild-type controls. This analysis also revealed that the density of these vesicles in the distal axons of *Borcs7*$^{Q87X/Q87X}$ neurons was higher than that in *Borcs7*$^{-/-}$ neurons but significantly lower than that in wild-type controls. Dynamic analysis of transport of LAMP1-positive particles along axons revealed a similar pattern, with wild-type neurons showing significantly higher velocity and run length than *Borcs7*$^{Q87X/Q87X}$ neurons, which in turn showed significantly higher values than *Borcs7*$^{-/-}$ neurons.

The phenotypic effects of homozygosity for the Q87X mutation are particularly apparent in neurons with long axons, and it seems likely that this is due to the susceptibility of these cells to disruption of the autophagy-lysosome pathway. Efficient fusion of lysosomes with late endosomes is dependent on the two organelles being transported to within sufficient proximity

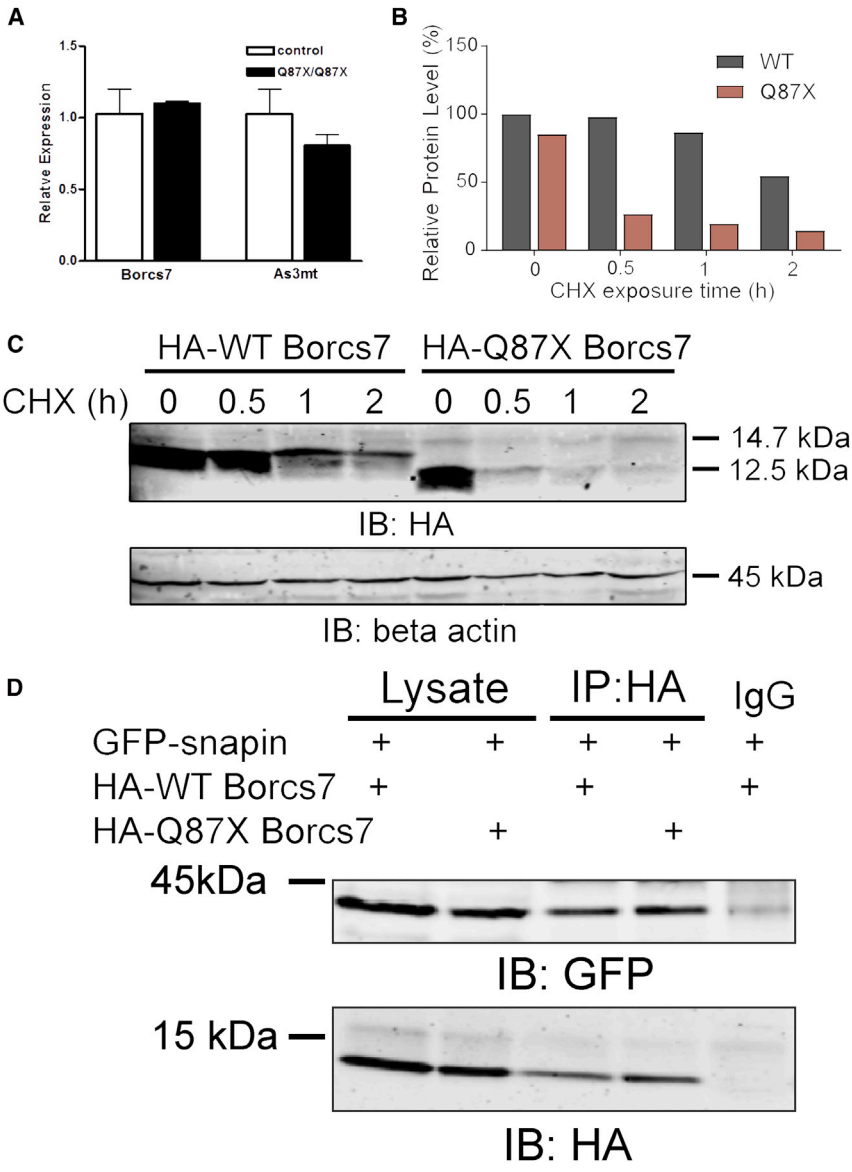

Figure 7. Effects of Q87X Truncation Mutation on Borcs7 Stability, Expression, and Interaction with Snapin

(A) Comparison of expression levels of *Borcs7* and *As3mt* in spinal cords of wild-type control and $Borcs7^{Q87X/Q87X}$ mice. Bars represent SEM.

(B and C) Cycloheximide chase assay comparing stability of WT BORCS7 to that of BORCS7-Q87X. Relative protein levels (%) of WT and Q87X BORCS7 were determined (B) by densitometric analysis of western blot (C).

(D) Immunoprecipitation (IP) assay comparing interaction of HA-tagged WT and BORCS7-Q87X with GFP-Snapin. Note that proteins were separated on a 14% polyacrylamide gel for the cycloheximide chase assay and a 6% polyacrylamide gel for the immunoprecipitation assay, thus allowing visualization of the difference in molecular weight between HA-tagged wild-type and Q87X Borcs7 in the former, but not the latter, assay.

of one another. This is illustrated by the effects of disruption of dynein-mediated centripetal movement of late endosomal cargo, which results in dispersion of late endocytic organelles to the cell periphery (Harada et al., 1998), proliferation of lysosomes, (Chevalier-Larsen et al., 2008), and impaired autophagic clearance of proteins prone to aggregation (Ravikumar et al., 2005). In neurons, disruption of retrograde dynein-driven endolysosomal traffic leads to axonal degeneration (Hafezparast et al., 2003; LaMonte et al., 2002). Mutations within the dynein heavy chain have been found to underlie spinal muscular atrophy with lower extremity predominance (SMA-LED), Charcot-Marie-Tooth disease type 2 (CMT2), microcephaly, and intellectual disability (reviewed in Schiavo et al., 2013), and mutations in the p150 subunit of dynactin have been linked to motor neuron disease (Münch et al., 2004; Puls et al., 2003, 2005). In the mutant mouse strain Loa, a mutation in the dynein tail results in impaired retrograde axonal transport and lower motor neuron degeneration as well as severe loss of sensory neurons (Chen et al., 2007; Ilieva et al., 2008). Rather than causing a decrease in instantaneous lysosome velocity during retrograde transport in axons, the Loa mutation was found to cause an increase in run terminations, resulting in a reduction in overall average lysosome velocity of 22% in mice heterozygous for the Loa mutation (Ori-McKenney et al., 2010). This suggests that the phenotype of our Q87X mice, similar to that of the Loa mice, may result from the observed decrease in lysosome velocity, but in the anterograde rather than retrograde direction. The deleterious effects of any resulting decrease in autophagic efficiency would be expected to be most apparent in cells with long axonal processes, such as motor neurons.

A number of molecular mechanisms may be proposed to explain the observed effects of the Q87X mutation on lysosome transport. The simplest model is one in which decreased stability of truncated Borcs7 results in a decrease in intracellular levels of the protein that are not compensated for by increased transcription. This could in turn decrease the cell's ability to form the BORCs necessary for anterograde transport of lysosomes. This model is supported by the results of a cycloheximide chase assay we performed, which indicate that the half-life of HA-tagged BORCS7-Q87X expressed from a transgene is greatly reduced relative to that of the wild-type version of the protein. This model can be tested more definitively in the future using an antibody capable of recognizing both the mutant and wild-type versions of endogenous BORCS7, thus allowing quantification of BORCS7 protein levels in neurons.

It is also possible that a deficit in the ability of BORCS7-Q87X to interact with the BORC contributed to the lysosomal trafficking deficit observed in *Borcs7*$^{Q87X/Q87X}$ neurons. This is indirectly supported by the fact that motor activity in *Borcs7*$^{Q87X/-}$ mice was not more severely affected than that in *Borcs7*$^{Q87X/Q87X}$ mice, suggesting that decreased protein levels alone are not sufficient to account for the observed phenotype. However, this is not supported by our immunoprecipitation study in HEK293T cells, where we found no measurable difference between BORCS7-Q87X and wild-type Borcs7 in their association with Snapin, indicating that the truncated protein is still able to be incorporated into the BORC. More in depth investigation will be required to determine whether the Q87X mutation compromises the ability of Borcs7 to carry out its normal function in the assembly of a functional BORC, despite the fact that it does not prevent the protein from associating with the complex.

EXPERIMENTAL PROCEDURES

Mouse Breeding

All animal colonies were maintained according to standard guidelines as defined by the NIH Guide for the Care and Use of Laboratory Animals and the Institutional Animal Care and Use Committee at University of North Carolina (UNC)-Chapel Hill. The mutation occurred spontaneously on a mixed background consisting of 129/SvEv, C57BL/6, and DBA/2. Wild-type C57BL/6 and BALB/cByJ mice were purchased from the Jackson Laboratory.

Nervous System Histopathology and Electron Microscopy

Tissue was fixed by perfusion with PBS followed by 4% paraformaldehyde (PFA), post-fixed overnight in 4% PFA at 4°C, and embedded in paraffin. 8-μM serial sections were stained with Luxol Fast Blue and cresyl violet. α-motor neurons were enumerated in the dorsal root of at least 21 serial sections made from the L1 region of the lumbar spinal cord. The right ventral horn from each section was photographed using 20× magnification, and only large cells with a clearly visible cytoplasm and nucleolus were counted. For electron microscopy (EM), tissue was fixed in 2% PFA, 2% glutaraldehyde, and 0.15 M $NaPO_4$ (pH 7.4).

Behavioral Testing

For the wire hang test for grip strength, mice were placed on the lid of a large metal cage, which was gently shaken to promote grip onto the grid. Subsequently, the cage top was flipped over and latency to fall was recorded. The maximum trial length was 60 s, and coordination during the task was also recorded using a scoring system in which zero indicated normal performance and −4 indicated severe instability.

Rotarod testing (Ugo Basile, Stoelting, Wood Dale, IL) was performed to test motor coordination and learning. During the acquisition session, mice were given three trials, each separated by 45-s intervals. Re-testing consisted of two trials. Revolutions per minute (rpm) was set at an initial value of 3, with a progressive increase to a maximum of 30 rpm across 5 min. Latency to fall from the top of the rotating barrel was assessed.

Locomotor activity was assessed over one-hour trial periods in an open-field chamber (41 × 41 × 30 cm) crossed by a grid of photobeams (VersaMax system; AccuScan Instruments). The number of photobeams broken during the trial was collected in five-minute intervals, with separate measures for distance traveled and rearing movements.

Mapping Protocols

Initial genome-wide SNP analysis was performed to identify an area of linkage. Following SNP analysis, fine mapping was conducted using microsatellite polymorphism screening. The published primer sets for D19Mit53, D19Mit10, D19Mit11.1, and D19Mit46 were purchased and used. Additionally, novel microsatellites were identified for analysis, and primers were made. Screening at 46.1 MB on Chr 19 was done with the forward primer 5′-AAACCAGATGCCAACCTCTAG-3′ and the reverse primer 5′-GTACCACTATGCCTGCTCATT-3′. A microsatellite at 47.09 MB was analyzed using the forward primer 5′-GCTAATGACAACTGCCTTGC-3′ and the reverse primer 5′-TAGATGGACAAGGAAACTGCG-3′.

Whole-Genome Sequencing

A DNA library was prepared using the KAPA DNA library kit. Size selection of the library was performed by agarose gel electrophoresis to assure a minimum 300 bp insert size. The DNA library was sequenced on two lanes of the Illumina HiSeq2000 through the Pair Ends 2 × 100 approach. The CLC Genomic Workbench package (currently QIAGEN) was used for adaptor sequence removal, alignment to the reference genome, and single nucleotide variant (SNV) call.

Construction of Vectors for Expressing Tagged Proteins

The coding sequences for KIF5A, Snapin, wild-type BORCS7, and BORCS7-Q87X were amplified by PCR from cDNA reverse transcribed from RNA isolated from whole brain as described under Expression Analysis. PCR primers were designed to add a SalI site to the 5′ end of the coding sequence and a BamHI site to the 3′ end to allow cloning between the XhoI and BamHI sites of the appropriate vectors for addition of a fluorescent or HA tag. For addition of a Scarlet tag to the amino terminus of proteins, cDNAs were cloned into pmScarlet_C1, which was a gift from Dorus Gadella (Addgene plasmid no. 85042). For addition of an EGFP tag, cDNAs were cloned into pEGFP-C1 (Clontech Laboratories).

Expression Analysis

Total RNA was isolated using an RNA isolation solvent (RNA-Bee; Tel-Test, Friendswood, TX, USA) according to the manufacturer's protocol. Reverse transcription of RNA to cDNA for qRT-PCR was performed using a high-capacity cDNA archive kit (Applied Biosystems) according to the manufacturer's instructions. Primers and probes were purchased from Applied Biosystems. DNA was amplified with Taqman PCR Universal Master Mix (Applied Biosystems, Foster City, CA, USA) using the Applied Biosystems 7900 HT Fast RT-PCR System. All samples were run in duplicate, and relative expression was determined by normalizing samples to 18S RNA (ΔCT). To facilitate use of this highly expressed internal standard, samples were diluted to 10 pg/μL for analysis with this primer set, compared to a dilution of 2.5 ng/μL for all other probe sets. Data were analyzed using the comparative threshold cycle (CT) method as described by Applied Biosystems.

Neuronal Culture and Transfection

Primary cortical neuronal cultures were prepared from 15- to 17-day-old embryos following a previously described methodology (Lorenzo et al., 2014). For time-lapse imaging experiments, DIV5 hippocampal neurons were transfected with 1 μg of each plasmid DNA after a modified Ca^{2+}-phosphate transfection protocol (Jiang and Chen, 2006) using the CalPhos Mammalian Transfection kit (Takara Bio) and imaged 48 hr after transfection. Neurons were processed for immunofluorescence 2 days after transfection.

Fluorescence Labeling of Neurons

Neuronal cultures were fixed and prepared for immunofluorescence as previously described (Lorenzo et al., 2014). Axons were identified by staining with a primary antibody against 480 kDa ankyrin-G (Jenkins et al., 2015) in blocking buffer overnight at 4°C. Cells were washed three times with PBS, incubated with fluorescent-labeled secondary antibody conjugates (Life Technology) in blocking buffer for 1 hr at room temperature, washed five times with PBS, and mounted in Vectashield mounting medium (Vector Laboratories). Lysosomal distribution was measured in a minimum of 25 fixed neurons per genotype.

Time-Lapse Video Microscopy and Video Analyses

Live microscopy of neuronal cultures was performed using a laser inverted scanning confocal microscope (LSM 780) equipped with a digital microscope AxioCam camera, a GaAsP detector, and a temperature- and CO2- controlled incubation chamber. Time-lapse images were collected from neuronal preparation incubated at 37°C and 5% CO_2 in phenol red-free Hibernate E and captured in the midaxon, ~60 μm away from the soma, with a 40× oil objective, 1.3 numerical aperture (NA), at a rate of 1 frame/s for time intervals ranging

from 60 to 300 s using the zoom and definite focus functions of the Zen 2011 acquisition and imaging software (Zen Black 2011). Time-lapse images were exported as 15 frames/s video files using the Zen 2011 acquisition and imaging software that were processed and analyzed using ImageJ (NIH). Kymographs were obtained using the KymoToolBox plugin for ImageJ (Zala et al., 2013). In addition, the KymoToolBox plugin was used to manually follow a subset of particles from each kymograph and reported the tracked particles on the original kymograph and video files using a color code for movement directionality (green for anterograde, red for retrograde, and blue for stationary particles). Quantitative analyses were performed manually by following the trajectories of individual particles to calculate dynamic parameters, including net and directional velocities and net and directional run length as well as time of pause or movement in a particular direction of transport. Anterograde and retrograde motile vesicles were defined as particles showing a net displacement >3 μm in one particular direction, and stationary vesicles were defined as particles with a net displacement <2 μm. A minimum of 20 movies were analyzed for each genotype.

Cycloheximide Chase Experiments

293T cells (HEK293) were cultured in DMEM supplemented with 10% fetal bovine serum (FBS). Cells were transfected with HA-tagged vectors expressing wild-type Borcs7 or truncated Q87X proteins using Lipofectamine 3000 (Invitrogen). 48 hr after transfection, cells were treated with 50 μM cycloheximide for the indicated times. Cell lysates were prepared using radioimmunoprecipitation assay (RIPA) buffer, and 60 μg protein was loaded for PAGE on a 14% gel. Western blotting was performed with mouse HA antibody (Covance) and anti-mouse infrared (IR) secondary (LI-COR Biosciences). Densitometry was performed using ImageJ.

Immunoprecipitation

For coimmunoprecipitation experiments, 6×10^6 HEK293T cells were plated in 10-cm dishes and transfected with 4 μg of each plasmid using Lipofectamine 2000 (Invitrogen) according to the manufacturer's instructions. Cells were harvested 48 hr after transfection and lysed in 0.5% Triton X-100 in lysis buffer (10 mM sodium phosphate, 0.32 M sucrose, 2 mM EDTA, and protease inhibitors). Cell lysates were centrifuged at 100,000 *g* for 30 min, and the soluble fraction was collected and precleared by incubation with protein G Dynabeads. Coimmunoprecipitation experiments were performed using protein G Dynabeads and mouse anti-HA (Covance) or in-house made rabbit anti-GFP (Lorenzo et al., 2014) antibodies. Immunoprecipitation samples were resolved by SDS-PAGE and western blot, and antibodies were detected using IRDye 800CW and IRDye 680RD secondary antibodies (LI-COR Biosciences).

SUPPLEMENTAL INFORMATION

Supplemental Information includes Supplemental Experimental Procedures and seven figures and can be found with this article online at https://doi.org/10.1016/j.celrep.2018.06.118.

ACKNOWLEDGMENTS

We thank Kara Agster Saddoris for assistance with the behavioral tests, Pablo Ariel and Victoria J. Madden for assistance with confocal microscopy and electron microscopy, Patricia Maness and Vishwa Mohan for assistance with neuronal cultures and immunohistochemistry, Eva Anton and Steven J. Gray for advice on phenotypic analysis of the mutant mice, Wendy Zinzow-Kramer and Rebecca Dye for assistance in breeding, Anne Latour for assistance with culture of embryonic stem cells, and the Animal Models Core for blastocyst injections. Studies using the Mouse Behavioral Phenotyping Core and Microscopy Core were supported by the Eunice Kennedy Shriver National Institute of Child Health and Human Development (NICHD) grant U54HD079124 to the UNC Intellectual and Developmental Disabilities Research Center. Work using the Microscopy Core was also supported by grant P30 NS045892 to the UNC Neuroscience Center. D.N.L. is supported in part by a Simmons Scholarship. We dedicate this work to the memory of Hannes Holzmüller.

AUTHOR CONTRIBUTIONS

Conceptualization, J.N.S., D.N.L., R.J.C., S.S.M., and B.H.K.; Methodology, J.N.S., D.N.L., R.J.C., M.N., S.S.M., P.M., and B.H.K.; Formal Analysis, D.N.L., R.J.C., L.J., M.N., S.S.M., D.A., and P.M.; Investigation, D.N.L., R.J.C., J.N.S., L.J., M.N., M.L.W., S.S.M., D.A., P.M., and F.P.M.d.V.; Original Draft, R.J.C., J.N.S., A.S., and S.S.M.; Writing – Review & Editing, R.J.C., J.N.S., A.S., S.S.M., D.N.L., and B.H.K.; Visualization, R.J.C., J.N.S., M.N., D.N.L., S.S.M., and B.H.K.; Supervision Oversight and Funding Acquisition, B.H.K., D.N.L., and S.S.M.

DECLARATION OF INTERESTS

The authors declare no competing interests.

Received: September 11, 2017
Revised: May 6, 2018
Accepted: June 28, 2018
Published: July 31, 2018

REFERENCES

Abeliovich, A., and Gitler, A.D. (2016). Defects in trafficking bridge Parkinson's disease pathology and genetics. Nature *539*, 207–216.

Blackstone, C., O'Kane, C.J., and Reid, E. (2011). Hereditary spastic paraplegias: membrane traffic and the motor pathway. Nat. Rev. Neurosci. *12*, 31–42.

Campbell, P.D., Shen, K., Sapio, M.R., Glenn, T.D., Talbot, W.S., and Marlow, F.L. (2014). Unique function of Kinesin Kif5A in localization of mitochondria in axons. J. Neurosci. *34*, 14717–14732.

Chen, X.J., Levedakou, E.N., Millen, K.J., Wollmann, R.L., Soliven, B., and Popko, B. (2007). Proprioceptive sensory neuropathy in mice with a mutation in the cytoplasmic Dynein heavy chain 1 gene. J. Neurosci. *27*, 14515–14524.

Chevalier-Larsen, E.S., Wallace, K.E., Pennise, C.R., and Holzbaur, E.L. (2008). Lysosomal proliferation and distal degeneration in motor neurons expressing the G59S mutation in the p150Glued subunit of dynactin. Hum. Mol. Genet. *17*, 1946–1955.

Crimella, C., Baschirotto, C., Arnoldi, A., Tonelli, A., Tenderini, E., Airoldi, G., Martinuzzi, A., Trabacca, A., Losito, L., Scarlato, M., et al. (2012). Mutations in the motor and stalk domains of KIF5A in spastic paraplegia type 10 and in axonal Charcot-Marie-Tooth type 2. Clin. Genet. *82*, 157–164.

Ebrahimi-Fakhari, D., Saffari, A., Wahlster, L., Lu, J., Byrne, S., Hoffmann, G.F., Jungbluth, H., and Sahin, M. (2016). Congenital disorders of autophagy: an emerging novel class of inborn errors of neuro-metabolism. Brain *139*, 317–337.

Farías, G.G., Guardia, C.M., De Pace, R., Britt, D.J., and Bonifacino, J.S. (2017). BORC/kinesin-1 ensemble drives polarized transport of lysosomes into the axon. Proc. Natl. Acad. Sci. USA *114*, E2955–E2964.

Fraldi, A., Klein, A.D., Medina, D.L., and Settembre, C. (2016). Brain disorders due to lysosomal dysfunction. Annu. Rev. Neurosci. *39*, 277–295.

Guardia, C.M., Farías, G.G., Jia, R., Pu, J., and Bonifacino, J.S. (2016). BORC functions upstream of kinesins 1 and 3 to coordinate regional movement of lysosomes along different microtubule tracks. Cell Rep. *17*, 1950–1961.

Hafezparast, M., Klocke, R., Ruhrberg, C., Marquardt, A., Ahmad-Annuar, A., Bowen, S., Lalli, G., Witherden, A.S., Hummerich, H., Nicholson, S., et al. (2003). Mutations in dynein link motor neuron degeneration to defects in retrograde transport. Science *300*, 808–812.

Haidar, M., and Timmerman, V. (2017). Autophagy as an emerging common pathomechanism in inherited peripheral neuropathies. Front. Mol. Neurosci. *10*, 143.

Harada, A., Takei, Y., Kanai, Y., Tanaka, Y., Nonaka, S., and Hirokawa, N. (1998). Golgi vesiculation and lysosome dispersion in cells lacking cytoplasmic dynein. J. Cell Biol. *141*, 51–59.

Ilieva, H.S., Yamanaka, K., Malkmus, S., Kakinohana, O., Yaksh, T., Marsala, M., and Cleveland, D.W. (2008). Mutant dynein (Loa) triggers proprioceptive

axon loss that extends survival only in the SOD1 ALS model with highest motor neuron death. Proc. Natl. Acad. Sci. USA *105*, 12599–12604.

Jenkins, P.M., Kim, N., Jones, S.L., Tseng, W.C., Svitkina, T.M., Yin, H.H., and Bennett, V. (2015). Giant ankyrin-G: a critical innovation in vertebrate evolution of fast and integrated neuronal signaling. Proc. Natl. Acad. Sci. USA *112*, 957–964.

Jiang, M., and Chen, G. (2006). High Ca2+-phosphate transfection efficiency in low-density neuronal cultures. Nat. Protoc. *1*, 695–700.

Kiriyama, Y., and Nochi, H. (2015). The function of autophagy in neurodegenerative diseases. Int. J. Mol. Sci. *16*, 26797–26812.

Komatsu, M., Waguri, S., Chiba, T., Murata, S., Iwata, J., Tanida, I., Ueno, T., Koike, M., Uchiyama, Y., Kominami, E., and Tanaka, K. (2006). Loss of autophagy in the central nervous system causes neurodegeneration in mice. Nature *441*, 880–884.

Korolchuk, V.I., Saiki, S., Lichtenberg, M., Siddiqi, F.H., Roberts, E.A., Imarisio, S., Jahreiss, L., Sarkar, S., Futter, M., Menzies, F.M., et al. (2011). Lysosomal positioning coordinates cellular nutrient responses. Nat. Cell Biol. *13*, 453–460.

Kragh, C.L., Ubhi, K., Wyss-Coray, T., and Masliah, E. (2012). Autophagy in dementias. Brain Pathol. *22*, 99–109.

LaMonte, B.H., Wallace, K.E., Holloway, B.A., Shelly, S.S., Ascaño, J., Tokito, M., Van Winkle, T., Howland, D.S., and Holzbaur, E.L. (2002). Disruption of dynein/dynactin inhibits axonal transport in motor neurons causing late-onset progressive degeneration. Neuron *34*, 715–727.

Li, M., Jaffe, A.E., Straub, R.E., Tao, R., Shin, J.H., Wang, Y., Chen, Q., Li, C., Jia, Y., Ohi, K., et al. (2016). A human-specific AS3MT isoform and BORCS7 are molecular risk factors in the 10q24.32 schizophrenia-associated locus. Nat. Med. *22*, 649–656.

Lorenzo, D.N., Badea, A., Davis, J., Hostettler, J., He, J., Zhong, G., Zhuang, X., and Bennett, V. (2014). A PIK3C3-ankyrin-B-dynactin pathway promotes axonal growth and multiorganelle transport. J. Cell Biol. *207*, 735–752.

Martini-Stoica, H., Xu, Y., Ballabio, A., and Zheng, H. (2016). The autophagy-lysosomal pathway in neurodegeneration: a TFEB perspective. Trends Neurosci. *39*, 221–234.

Menzies, F.M., Fleming, A., Caricasole, A., Bento, C.F., Andrews, S.P., Ashkenazi, A., Füllgrabe, J., Jackson, A., Jimenez Sanchez, M., Karabiyik, C., et al. (2017). Autophagy and neurodegeneration: pathogenic mechanisms and therapeutic opportunities. Neuron *93*, 1015–1034.

Mrakovic, A., Kay, J.G., Furuya, W., Brumell, J.H., and Botelho, R.J. (2012). Rab7 and Arl8 GTPases are necessary for lysosome tubulation in macrophages. Traffic *13*, 1667–1679.

Münch, C., Sedlmeier, R., Meyer, T., Homberg, V., Sperfeld, A.D., Kurt, A., Prudlo, J., Peraus, G., Hanemann, C.O., Stumm, G., and Ludolph, A.C. (2004). Point mutations of the p150 subunit of dynactin (DCTN1) gene in ALS. Neurology *63*, 724–726.

Navone, F., Genevini, P., and Borgese, N. (2015). Autophagy and neurodegeneration: insights from a cultured cell model of ALS. Cells *4*, 354–386.

Nicolas, A., Kenna, K.P., Renton, A.E., Ticozzi, N., Faghri, F., Chia, R., Dominov, J.A., Kenna, B.J., Nalls, M.A., Keagle, P., et al. (2018). Genome-wide analyses identify KIF5A as a novel ALS gene. Neuron *97*, 1268–1283.e6.

Ori-McKenney, K.M., Xu, J., Gross, S.P., and Vallee, R.B. (2010). A cytoplasmic dynein tail mutation impairs motor processivity. Nat. Cell Biol. *12*, 1228–1234.

Pu, J., Schindler, C., Jia, R., Jarnik, M., Backlund, P., and Bonifacino, J.S. (2015). BORC, a multisubunit complex that regulates lysosome positioning. Dev. Cell *33*, 176–188.

Puls, I., Jonnakuty, C., LaMonte, B.H., Holzbaur, E.L., Tokito, M., Mann, E., Floeter, M.K., Bidus, K., Drayna, D., Oh, S.J., et al. (2003). Mutant dynactin in motor neuron disease. Nat. Genet. *33*, 455–456.

Puls, I., Oh, S.J., Sumner, C.J., Wallace, K.E., Floeter, M.K., Mann, E.A., Kennedy, W.R., Wendelschafer-Crabb, G., Vortmeyer, A., Powers, R., et al. (2005). Distal spinal and bulbar muscular atrophy caused by dynactin mutation. Ann. Neurol. *57*, 687–694.

Ravikumar, B., Acevedo-Arozena, A., Imarisio, S., Berger, Z., Vacher, C., O'Kane, C.J., Brown, S.D., and Rubinsztein, D.C. (2005). Dynein mutations impair autophagic clearance of aggregate-prone proteins. Nat. Genet. *37*, 771–776.

Reddy, A., Caler, E.V., and Andrews, N.W. (2001). Plasma membrane repair is mediated by Ca(2+)-regulated exocytosis of lysosomes. Cell *106*, 157–169.

Schiavo, G., Greensmith, L., Hafezparast, M., and Fisher, E.M. (2013). Cytoplasmic dynein heavy chain: the servant of many masters. Trends Neurosci. *36*, 641–651.

Schmidt, R.E., Dorsey, D., Parvin, C.A., Beaudet, L.N., Plurad, S.B., and Roth, K.A. (1997). Dystrophic axonal swellings develop as a function of age and diabetes in human dorsal root ganglia. J. Neuropathol. Exp. Neurol. *56*, 1028–1043.

Schreij, A.M., Fon, E.A., and McPherson, P.S. (2016). Endocytic membrane trafficking and neurodegenerative disease. Cell. Mol. Life Sci. *73*, 1529–1545.

Tian, J.H., Wu, Z.X., Unzicker, M., Lu, L., Cai, Q., Li, C., Schirra, C., Matti, U., Stevens, D., Deng, C., et al. (2005). The role of Snapin in neurosecretion: snapin knock-out mice exhibit impaired calcium-dependent exocytosis of large dense-core vesicles in chromaffin cells. J. Neurosci. *25*, 10546–10555.

Walkley, S.U., Sikora, J., Micsenyi, M., Davidson, C., and Dobrenis, K. (2010). Lysosomal compromise and brain dysfunction: examining the role of neuroaxonal dystrophy. Biochem. Soc. Trans. *38*, 1436–1441.

Watanabe, F., Arnold, W.D., Hammer, R.E., Ghodsizadeh, O., Moti, H., Schumer, M., Hashmi, A., Hernandez, A., Sneh, A., Sahenk, Z., and Kisanuki, Y.Y. (2013). Pathogenesis of autosomal dominant hereditary spastic paraplegia (SPG6) revealed by a rat model. J. Neuropathol. Exp. Neurol. *72*, 1016–1028.

Yang, D.S., Lee, J.H., and Nixon, R.A. (2009). Monitoring autophagy in Alzheimer's disease and related neurodegenerative diseases. Methods Enzymol. *453*, 111–144.

Zala, D., Hinckelmann, M.V., Yu, H., Lyra da Cunha, M.M., Liot, G., Cordelières, F.P., Marco, S., and Saudou, F. (2013). Vesicular glycolysis provides on-board energy for fast axonal transport. Cell *152*, 479–491.

Zhang, A., He, X., Zhang, L., Yang, L., Woodman, P., and Li, W. (2014). Biogenesis of lysosome-related organelles complex-1 subunit 1 (BLOS1) interacts with sorting nexin 2 and the endosomal sorting complex required for transport-I (ESCRT-I) component TSG101 to mediate the sorting of epidermal growth factor receptor into endosomal compartments. J. Biol. Chem. *289*, 29180–29194.

Zhou, W., He, Q., Zhang, C., He, X., Cui, Z., Liu, F., and Li, W. (2016). BLOS2 negatively regulates Notch signaling during neural and hematopoietic stem and progenitor cell development. eLife *5*, e18108.